Journal of Materials Chemistry C

ROYAL SOCIETY OF CHEMISTRY

PAPER

View Article Online
View Journal | View Issue

Cite this: J. Mater. Chem. C, 2024, 12, 11569

Tailoring thermal expansion and luminescence thermometric performance of $KMgScW_3O_{12}$-based compounds†

Ming Li,[a] Qi Miao,[a] Kaiyue Zhao,[a] Yangke Cun,*[b] Yongqiang Qiao,[a] Juan Guo,[a] Li Li*[c] and Qilong Gao *[a]

Negative thermal expansion (NTE) compounds provide an opportunity to understand the nature of thermal expansion and the engineering applications of inorganic solid functional materials. However, very few NTE materials have been found so far, which also restricts the unique applications of anomalous lattice effects in solving luminescence thermal quenching and ratio fluorescence temperature measurement. In this work, we have prepared $(KMg)_xSc_{2-x}W_3O_{12}$-based compounds with abnormal thermal expansion and luminescence negative thermal quenching. Their crystal structure, microstructure, thermal expansion properties, and semiconductor performance are studied by variable temperature X-ray diffraction, scanning electron microscopy, low-temperature differential scanning calorimetry, and UV-vis diffuse reflection spectroscopy. The thermal expansion can switch from positive to zero to negative by controlling the content of $(KMg)^{3+}$ ions. Interestingly, the upconversion luminescence spectra intensity in $(KMg)_xSc_{2-x}W_3O_{12}$-based compounds displays unique negative thermal quenching, including weak negative thermal quenching and strong thermal quenching with the x from 0.4 to 0.8. The results of decay curves show that the trend of decay curves with temperature is consistent with the thermal expansion behaviour; the stronger the NTE properties, the stronger the luminescence negative thermal quenching. The maximum absolute sensitivity (S_a) of $(KMg)_{0.4}Sc_{1.42}W_3O_{12}$:0.15Yb/0.03Er is 0.50 × 10^{-2} K^{-1} at 385 K, and the maximum relative sensitivity (S_r) is 0.86% K^{-1} at 298 K. This work does not only provide a new NTE material but also find that the NTE material as a luminescent host can produce a phenomenon of luminescence thermal enhancement.

Received 22nd February 2024,
Accepted 18th June 2024

DOI: 10.1039/d4tc00711e

rsc.li/materials-c

1. Introduction

Most materials display thermal expansion under heating, called positive thermal expansion (PTE). However, a few materials exhibit the characteristics of "thermal shrinkage or cold expansion", which are named negative thermal expansion (NTE) materials. These have attracted increasing attention in some fields of precision control of thermal expansion, such as optical fiber reflective grating devices and circuit boards, which could act as an additive to control the thermal expansion of matrix materials.[1] So far, NTE compounds can be roughly divided into two broad categories: one is driven by low-frequency phonons, such as oxides,[2,3] fluorides,[4,5] cyanides,[6,7] and MOFs.[8,9] Another is the class of electron-driven NTE compounds, such as $BiNiO_3$,[10] $BiCu_3Fe_4O_{12}$,[11] Mn_3AN,[12] and alloys.[13] It should be noted that most phonon-driven NTE materials have a wider NTE temperature window, even exceeding 1000 K, such as ZrW_2O_8,[14] $Y_2W_3O_{12}$,[15] ScF_3,[16] and $CaZrF_6$.[17] Among them, the $A_2M_3O_{12}$ series NTE materials have been extensively studied due to their large coefficient of thermal expansion (CTE) and flexible chemical structure.[18,19] However, $A_2M_3O_{12}$ with smaller A^{3+} cations (*e.g.* Fe^{3+}, Al^{3+}, and Cr^{3+}) has a higher phase transition temperature, and its NTE behaviour is only displayed after a monoclinic-orthogonal phase transition.[20,21] For larger A^{3+} cations (such as Y^{3+}, Yb^{3+}, Er^{3+}, and Lu^{3+}), the sample easily absorbs water,[18,22] and its NTE properties are only displayed after the release of crystal water. $NaZr_2P_3O_{12}$ (NZP) has a 3D framework structure with a ZrO_6 octahedron corner linked to a PO_4 tetrahedron,[23] possessing hexagonal symmetry.[24] Due to high structural flexibility, it also has excellent ionic conductor properties. Meanwhile, this structure is already known for the possibility of ionic substitution to create new materials with desired properties. Additionally, some NZP members present high mechanical strength, good chemical stability, high

[a] School of Physics and Microelectronics, Zhengzhou University, Zhengzhou, 450001, China. E-mail: qilonggao@zzu.edu.cn
[b] College of Materials Science and Engineering, Kunming University of Science and Technology, Kunming 650093, China. E-mail: cunyangke@126.com
[c] College of Science, Chongqing University of Posts and Telecommunications, Chongqing 400065, P. R. China. E-mail: lilic@cqupt.edu.cn

† Electronic supplementary information (ESI) available. See DOI: https://doi.org/10.1039/d4tc00711e

melting point, great hardness, and radiation resistance.[25] In some cases, it has a detrimental effect on mechanical strength because it causes microstresses and consequently microcracks.[26] Therefore, it is much more important to explore strong NTE oxides over a wide temperature range.

It is well known that upconversion luminescence (UCL) of RE^{3+} doped materials can convert near-infrared light to visible light and even ultraviolet (UV) light, and they have a large application market in anti-counterfeiting, photodynamic therapy, and temperature sensing.[27] However, the use of luminescent materials is largely limited by thermal quenching (TQ), that is, the luminescence intensity decreases with increasing temperature. Therefore, maintaining or even enhancing the luminescence at high temperatures is of high technological importance. A lot of attempts have been made to improve the luminescence properties of UC materials, such as adding sensitizers, tailoring the local crystal field, controlling the particle size, and tuning the phase of host materials;[28–31] these attempts to combat TQ have only met with limited success. Wang *et al.* used $Yb_2W_3O_{12}$ and $Sc_2Mo_3O_{12}$ as luminescent host materials to exhibit thermal enhanced UC emission of rare-earth ions (*i.e.*, Er^{3+}, Ho^{3+}) due to contraction and distortion of the host lattice with increasing temperature; the lattice contraction brings a reduction in the distance between sensitizers (Yb^{3+}) and activators (Er^{3+}), which contributes to the energy transfer (ET) from Yb^{3+} to Er^{3+} leading to enhancement of the UCL intensity.[32] These results provide an idea of utilizing the advantages of NTE compounds to design various luminescent materials with excellent luminescence stability. However, the explanations that NTE materials can solve TQ are different. Liao *et al.* studied the luminescence properties of $Sc_2Mo_3O_{12}$:Yb^{3+}/Er^{3+} and explained that the thermally enhanced UC emission is mainly controlled by the ET from Yb^{3+} to Er^{3+} at 298–473 K and then by the radiation transition of Er^{3+} above 473 K.[33] Huang *et al.* explained that the formation of a Yb-MoO_4 dimer leads to the tunable ET process of $Yb_2Mo_3O_{12}$:Yb^{3+}/Er^{3+}.[34] Wei *et al.* reported that the Frenkel defect formed *via* controlled annealing of $Sc_2(WO_4)_3$:Ln (Ln = Yb, Er, Eu, Tb, and Sm) can work as an energy reservoir and back-transfer the stored excitation energy to Ln^{3+} upon heating.[35] Nevertheless, the investigation on the thermal enhancement of UC emission as well as its corresponding mechanism in rare-earth ion doped NTE compounds is still not sufficient and the connection between NTE intensity and luminescence intensity is not clearly stated.

In this work, we have prepared a series of new NTE materials $(KMg)_xSc_{1.82-x}W_3O_{12}$:0.15Yb/0.03Er ($x$ = 0.4, 0.6, and 0.8), which do not undergo phase transitions throughout the test temperature range. Since Yb^{3+} can obtain near-infrared excitation at 980 nm and has a large absorption cross-section, and ET for other rare earth ions is high,[36–38] Yb^{3+} is selected as the sensitizer and Er^{3+} as the activator. The structure and lattice dynamics of $(KMg)_xSc_{1.82-x}W_3O_{12}$:0.15Yb/0.03Er ($x$ = 0.4, 0.6, and 0.8) are revealed by variable temperature X-ray diffraction (XRD), Raman testing, field emission scanning electron microscopy (SEM) and differential scanning calorimetry (DSC) to understand the NTE mechanism. UV-vis absorption spectroscopy and density functional theory (DFT) calculations show that the $KMgScW_3O_{12}$ sample has semiconductor properties. An Edinburgh FLS1000 steady-state fluorescence spectrometer connected to a temperature controller (HFS600E-PB2) is used to record the fluorescence spectra and decay curves. The temperature sensing performance of Er^{3+} is studied in the range of 298–748 K by monitoring the fluorescence intensity ratio (FIR) of $^2H_{11/2}$ and $^4S_{3/2}$ thermally coupled energy levels (TCLs). At 385 K, the maximum absolute sensitivity (S_a) is 0.50 × 10^{-2} K^{-1}. At 298 K, the maximum relative sensitivity (S_r) is 0.86% K^{-1}. The results show that NTE materials have great application prospects in luminescence. For convenience, the $(KMg)_xSc_{1.82-x}W_3O_{12}$:0.15Yb/0.03Er ($x$ = 0.4, 0.6, and 0.8) samples are recorded as KM4, KM6, and KM8 in the following analysis.

2. Results and discussion

2.1 Structure, composition, and morphology analysis

Fig. 1(a) shows the crystal structure of the KM4 sample. The material has a hexagonal structure with the space group $R\bar{3}c$ (No. 167), which is consistent with those of NZP materials.[39] The structure of the KM4 sample consists of a [Sc(Mg)O_6] octahedron and a [WO_4] tetrahedron, which is connected by a shared O atom, and K^+ ions independently embedded in the voids of the crystal structure. As shown in Fig. 1(b), the XRD patterns of KM4, KM6, and KM8 samples are consistent with that of the $KMgScMo_3O_{12}$ standard card (PDF card number 04-025-3546). There are no more or less peaks, indicating that the synthesized sample is pure phase. We perform Rietveld refinement on the crystal structure of the KM4 sample. It has good crystallinity, and the pattern can be well refined by the $R\bar{3}c$ space group. The lattice parameters after refinement are $a = b$ = 9.53897 Å, c = 24.41263 Å, and V = 1923.748 $Å^3$ (Fig. 1c). The room temperature (RT) XRD refinement results of KM6 and KM8 samples are shown in Fig. S1 (ESI†). Fig. 1(d) shows the changes in unit cell parameters and volume of $(KMg)_xSc_{1.82-x}W_3O_{12}$:0.15Yb/0.03Er with the content of $(KMg)^{3+}$ ions. The unit cell parameters and volume of the samples change linearly with the increase of $(KMg)^{3+}$ ions, and the unit cell volume decreases with the increase of the doping ion content. This is due to the replacement of the larger Sc^{3+} ion (R = 0.75 Å, CN = 6, R is the ionic radius and CN is the coordination number) by the smaller Mg^{2+} ion (R = 0.72 Å, CN = 6). These results show that Mg^{2+} ions are replaced at the Sc^{3+} site, leading to a slight contraction of the unit cell volume.

The SEM image and the elemental distribution diagram of the KM4 sample are shown in Fig. 2. It displays the irregular blocky structure because of high aggregation under high-temperature calcination. Fig. 2(b)–(h) show the elemental mapping of K, Mg, Sc, W, O, Yb, and Er, and the elements are uniformly distributed in the sample. In addition, XPS analysis is used to determine the valence states of the component elements in the KM4 sample (Fig. S2, ESI†). The valence states of K, Mg, Sc, and Yb are +1, +2, +3, and +3, respectively.

2.2 Thermal expansion performance

In order to extract the thermal expansion behaviour, the intrinsic thermal expansion of the KM4 sample (300–800 K) was

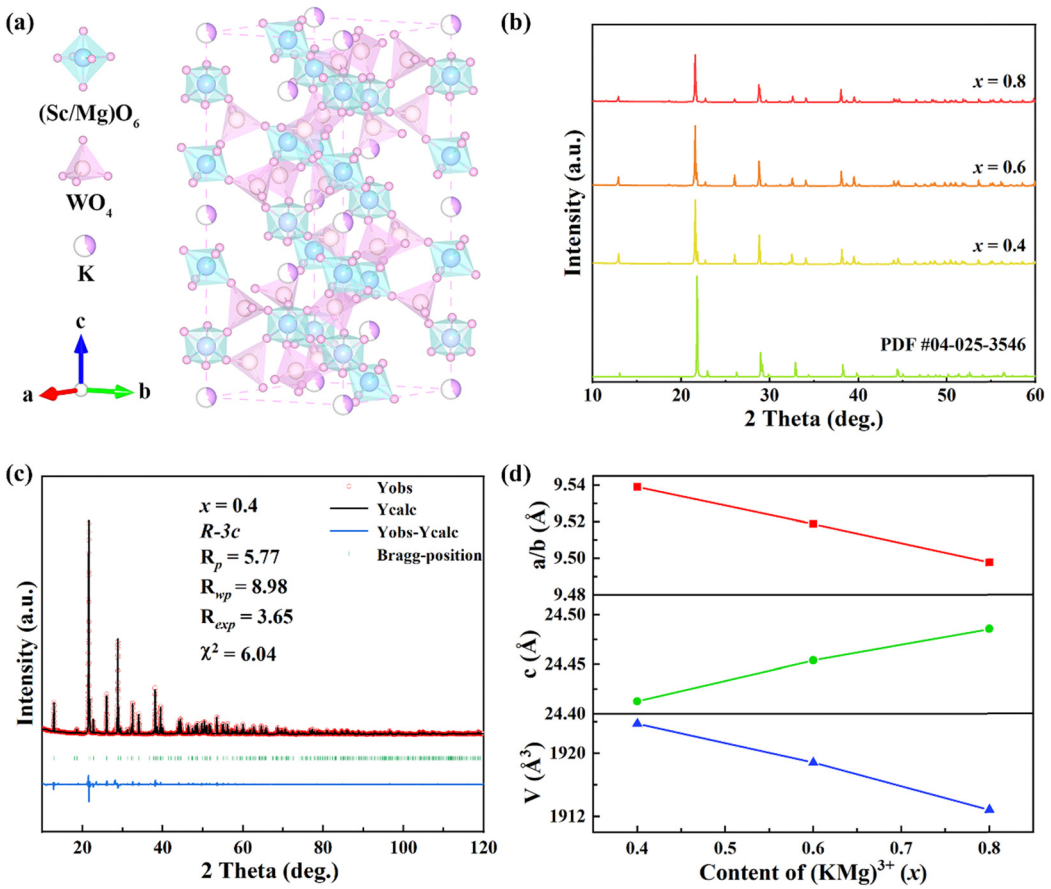

Fig. 1 (a) Crystal structure of the KM4 sample. (b) The XRD patterns for KM4, KM6, and KM8 samples at RT. (c) Rietveld refinement results of the XRD pattern at RT of the KM4 sample. (d) Lattice constants of KM4, KM6, and KM8 samples.

investigated using a variable temperature XRD test (Fig. 3a). The results of variable temperature XRD also suggest that the sample maintains a hexagonal phase structure and has good thermal stability. The illustration shows the diffraction peak (1 1 3) between 21.4° to 21.6° shifts first to the left (300–350 K) and then to the right (350–800 K). We can extract unit cell parameters and volume of the KM4 sample by Rietveld refinement with the Fullprof software, as shown in Fig. 3(b). The detailed unit cell parameters and structural parameters are shown in Tables S1–S3 (ESI†). The thermal expansion of the sample shows anisotropy, contraction of the a/b axis, and expansion of the c-axis. The CTEs of the a, b, and c axes are $\alpha_a = \alpha_b = -7.4 \times 10^{-6}\ K^{-1}$ and $\alpha_c = 15.5 \times 10^{-6}\ K^{-1}$, respectively. The volume CTE is $\alpha_v = -3.4 \times 10^{-6}\ K^{-1}$. It should be noted that it shows PTE (300–350 K) and NTE (350–800 K). The initial shift of the diffraction peak to the left may be due to the presence of trace amounts of crystal water

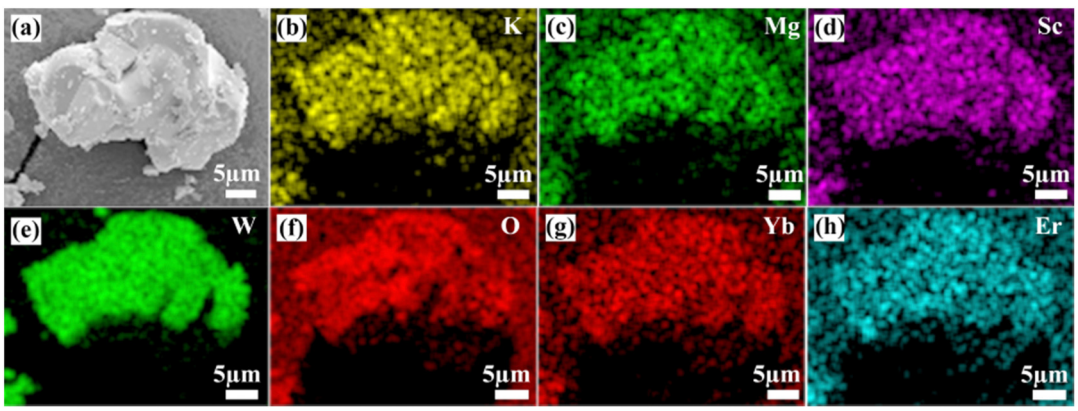

Fig. 2 (a) SEM image and (b)–(h) elemental mapping images of K, Mg, Sc, W, O, Yb, and Er elements for the KM4 sample.

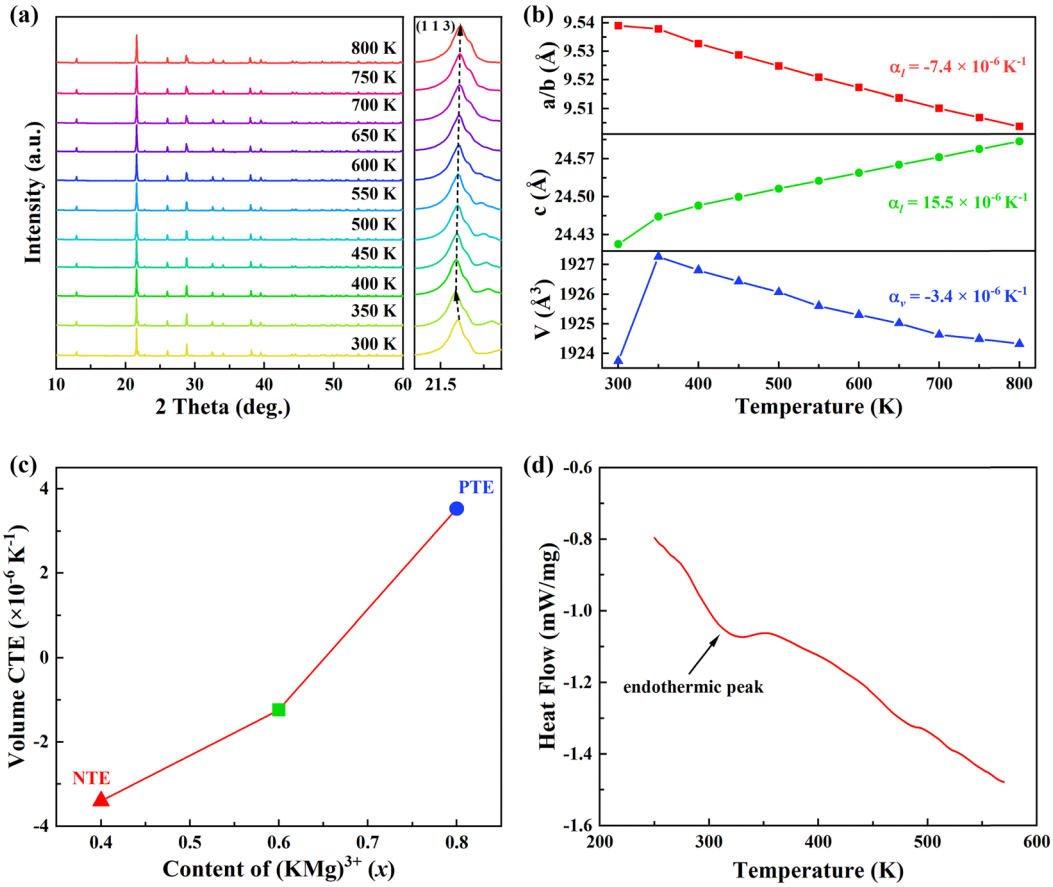

Fig. 3 (a) Temperature-dependent XRD patterns and local amplification of the KM4 sample (300–800 K). (b) Temperature dependence of lattice parameters and unit cell volume of the KM4 sample. (c) The CTEs of KM4, KM6, and KM8 samples vary with $(KMg)^{3+}$ ions. (d) DSC data of the KM4 sample.

in the sample.[22] The volume CTEs of KM6 and KM8 are α_v = -1.2×10^{-6} K^{-1} and $\alpha_v = 3.5 \times 10^{-6}$ K^{-1}, respectively (Fig. S3 and S4, ESI†). Therefore, we can achieve adjustable CTEs by changing the composition ratio of the samples. In addition, compared with samples showing zero thermal expansion (ZTE) such as $(Sc_{0.85}Ga_{0.05}Fe_{0.1})F_3$ ($\alpha_l = 0.2 \times 10^{-6}$ K^{-1}, 300–900 K),[40] $NiPt(CN)_6$ ($\alpha_l = -1.02(11) \times 10^{-6}$ K^{-1}, 100–330 K),[41] and $FeCo(CN)_6$ ($\alpha_l = -1.5 \times 10^{-6}$ K^{-1}, 4.2–300 K),[42] the synthesis method of KM4, KM6 and KM8 samples is simpler and more convenient, and the temperature window is much wider. Fig. 3(c) further shows the change of CTEs of the samples with the content of $(KMg)^{3+}$ ions. The CTEs of KM4, KM6, and KM8 samples change from negative to zero to positive with the increase of $(KMg)^{3+}$ ions. The explanation for this phenomenon is that Mg^{2+} ions occupy the position of Sc^{3+} ions, and K^+ ions are separately embedded in the voids of the structure. As x increases from 0.4 to 0.8, more and more spaces in the crystal structure of the sample are occupied by K^+ ions, which weakens the flexibility and reduces the space for the coupling rotation of the material, resulting in the weakening of NTE performance. This thermal expansion behavior also was observed in $Na_xGaFe(CN)_6$ and $Li_x(Sc,Fe)_3$ systems.[16,43] In Fig. 3(d), the endothermic peak at 300–350 K corresponds exactly to the increase in sample volume in Fig. 3(b), so it is speculated that the sample might contain crystal water. After 350 K, the crystal water is completely released and the sample begins to exhibit its own NTE properties. In summary, when x = 0.4, the NTE performance of the sample is the strongest.

2.3 NTE mechanism of KM4

In order to further reveal the mechanism of NTE, bond angles and bond lengths of KM4 are extracted from 300 to 800 K. Fig. 4(a) shows that the KM4 sample has only two kinds of bond angles: Sc5–O1–W3 and Sc5–O2–W3. Sc atoms and W atoms are connected by O1 and O2 to form a Sc–O–W atomic chain and coupled with O atoms for rotation. In order to reveal the NTE of the a/b axis and the PTE of the c-axis, the changes of Sc5–O1–W3 and Sc5–O2–W3 bond angles with temperature are analyzed, as shown in Fig. 4(b). With the increase in temperature, the Sc5–O1–W3 bond angle decreases from 147° to 143.2°, and the Sc5–O2–W3 bond angle decreases from 152.3° to 145.8°, that is, both bond angles decrease. The detailed bond angle information is given in Table S4 (ESI†). The content of $(KMg)^{3+}$ ions in the KM4 sample is the least among a series of KM4, KM6, and KM8 samples, and there are relatively many gaps in the crystal structure, which makes the material space more flexible and the degree of material coupling rotation the highest. Fig. 4(c) analyzes the variation of the distance between the nearest

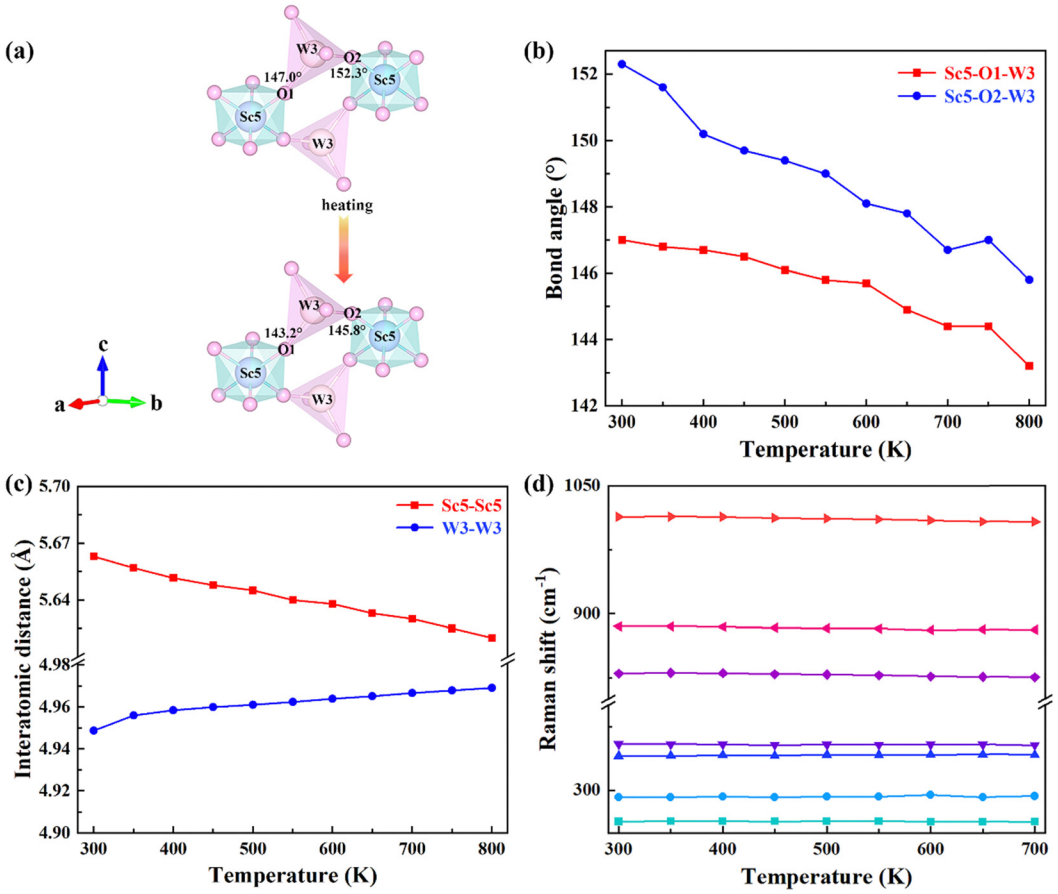

Fig. 4 KM4 sample. (a) Local lattice diagram of Sc5–O1–W3 and Sc5–O2–W3 bond angles from 300 K to 800 K. (b) The bond angles of Sc5–O1–W3 and Sc5–O2–W3 as a function of temperature. (c) The distance between the closest Sc atom and the closest W atom as a function of temperature. (d) Raman mode frequency shifts as a function of temperature for KM4.

identical atoms of the KM4 sample with temperature. The distance between Sc5 atoms decreases from 5.6630 Å to 5.6200 Å, and the distance between W3 atoms increases from 4.9487 Å to 4.9692 Å. The detailed bond length information is shown in Table S5 (ESI†). Because both Sc5–O1–W3 and Sc5–O2–W3 bond angles decrease with the increase of temperature, it results in the crystal structure stretching diagonally upward with the increase of temperature according to Fig. 4(a), resulting in contraction of the *ab* plane and elongation in the *c*-axis direction.

The negative thermal expansion of a framework structure originates from the phonon anharmonic vibrations. Raman spectroscopy has proved to be a powerful tool for studying phonon behaviours, providing information on shifts/broadening of phonon modes with pressure and temperature. Generally, Raman mode frequency undergoes a redshift (softening) with increasing temperature. Anomalous changes in Raman mode indicate negative thermal expansion. Blue shifts (stiffening) are observed at 291 cm^{-1} and 340 cm^{-1} (Fig. 4d). As shown in Fig. 4(d), the Raman peaks at 291 cm^{-1} and 340 cm^{-1} are assigned to the bending vibrations of MoO_4 groups.[44] This indicates that these modes have contributed to negative thermal expansion.[45,46] It should be noted that other Raman modes also have very little total anharmonicity, indicating that the coefficient of thermal expansion is little. This behaviour was also observed by other zero or low thermal expansion materials.[47,48]

Fig. S5(b) (ESI†) shows the shift of diffraction peaks corresponding to KM4, KM6, and KM8 samples with $(KMg)^{3+}$ ions at RT. The vibration modes at 263 cm^{-1}, 292 cm^{-1}, and 354 cm^{-1} move toward higher wavenumbers with the increase of the $(KMg)^{3+}$ content. The increase in wavenumber represents the hardening of chemical bonds, which will reduce the structural flexibility of the samples and is not beneficial for NTE.[49,50] Therefore, the KM8 sample with the highest content of $(KMg)^{3+}$ shows PTE. With the decrease of $(KMg)^{3+}$ ions, the thermal expansion performance of the sample changes from positive to negative.

2.4 Semiconductor properties of the $KMgScW_3O_{12}$ sample

In addition, the band gap of $KMgScW_3O_{12}$ has been investigated by UV-vis absorption spectroscopy. The band gap E_g is obtained by using the Tauc plot method, which is mainly based on the formula proposed by scholars such as Tauc, Davis, and Mott:[51]

$$(\alpha h\nu)^{\frac{1}{n}} = B(h\nu - E_g) \quad (1)$$

where α is the absorption coefficient, h is Planck's constant, ν is the incident light frequency, B is the proportionality constant, E_g

is the band gap width of the semiconductor, and n is dependent on the type of semiconductor (n = 1/2 for direct band gap semiconductors, n = 2 for indirect band gap semiconductors). As shown in Fig. 5(a), the band gap is estimated to be about ~4.24 eV according to the Tauc plot method, which shows the wide band gap semiconductor characteristics. The results of the DFT calculations indicate that $KMgScW_3O_{12}$ is an indirect band gap semiconductor with a band gap of 4.17 eV (Fig. 5b), which is smaller than the experimental value. This may be due to the fact that DFT calculations tend to underestimate the real band gap of materials.[52] The above results show that $KMgScW_3O_{12}$ has semiconductor properties, so it has the potential to be used as a material for making semiconductor devices.

2.5 Luminescence properties and temperature sensing performance of the synthesized particles

In order to investigate the effect of thermal expansion characteristics on the luminescence performance, the UCL spectra of KM4, KM6, and KM8 samples over the temperature range of 298–748 K are studied under the excitation of a 980 nm laser. Fig. 6(a) shows the UC emission spectra of the KM4 sample with temperature change. The sample has three distinct UC emission bands in the 500–700 nm range, which are derived from the electron emission transition of the activator (Er^{3+}) ion. The green emission bands centered at 521 nm/535 nm and 547 nm/558 nm are generated by the emission transitions of the $^2H_{11/2(2)}/^2H_{11/2(1)}$ and $^4S_{3/2(2)}/^4S_{3/2(1)}$ energy levels by the Er^{3+} ion ($^2H_{11/2}$ and $^4S_{3/2}$) energy level split, respectively.[53,54] The $^2H_{11/2}$ and $^4S_{3/2}$ energy levels are traditional thermally coupled energy levels, and any pair of energy levels $^2H_{11/2(2)}/^2H_{11/2(1)}$ and $^4S_{3/2(2)}/^4S_{3/2(1)}$ energy levels are thermally coupled energy levels due to the small energy gap.[55] A weak red emission with a central wavelength of 655 nm leads to an electron emission transition from the Er^{3+} ion ($^4F_{9/2} \rightarrow {}^4I_{15/2}$).[56] The spectral position of the KM4 sample is almost not affected by temperature, but the luminescence intensity increases with the increase of temperature, which is different from the TQ phenomenon in many rare earth ion doped luminescent materials.[57] In Fig. 6(b), the green UC emission intensity at 521 nm is increased by about 300 times, the green UC emission intensity at 547 nm is increased by about 80 times, and the corresponding total green UC emission intensity ($^2H_{11/2}$ + $^4S_{3/2}$) is increased by about 380 times (298–748 K). Er^{3+} ions have excellent green light emission, while the red light emission band is relatively weak from spectra. The change of green emission intensity corresponding to 521 nm in the UCL spectra of samples of different proportions with temperature is analyzed, as shown in Fig. 6(c). The data shown in the figure have been logarithmically processed. The green emission enhancement of the KM4 sample is the strongest, while the green emission of the KM8 sample is first enhanced and then weakened. This phenomenon shows that the stronger the NTE performance, the stronger the luminescence performance of the sample. Fig. 6(d) shows the possible UCL emission mechanism of a sample with the temperature at 298–748 K under 980 nm laser excitation. Yb^{3+} ions absorb energy from a 980 nm laser excited from the ground state $^2F_{7/2}$ to the $^2F_{5/2}$ level, transfer energy to neighboring Er^{3+} ions and then return to the ground state $^2F_{7/2}$. ET occurs between Yb^{3+} and Er^{3+} ions and energy is transferred to Er^{3+}:$^4I_{11/2}$ (ET1), $^4F_{9/2}$ (ET2), and $^4F_{7/2}$ (ET3). Er^{3+} ions from the ground state $^4I_{15/2}$ level transition to the $^4I_{11/2}$ energy level (ET1), and Er^{3+} ions from the $^4I_{13/2}$ level transition to the $^4F_{9/2}$ level (ET2). Er^{3+} ions transition from the $^4I_{11/2}$ level to the $^4F_{7/2}$ level and undergo rapid relaxation from the $^4F_{7/2}$ level to the $^2H_{11/2(2)}/^2H_{11/2(1)}$ and $^4S_{3/2(2)}/^4S_{3/2(1)}$ energy levels (ET3). Finally, the green emission bands (521 nm/535 nm and 547 nm/558 nm) can be attributed to the transitions of Er^{3+}: $^2H_{11/2(2)}/^2H_{11/2(1)} \rightarrow {}^4I_{15/2}$ and $^4S_{3/2(2)}/^4S_{3/2(1)} \rightarrow {}^4I_{15/2}$. The red radiation (655 nm) is produced by the Er^{3+}: $^4F_{9/2} \rightarrow {}^4I_{15/2}$ transition. The energy transfer depends directly on the sixth power (R^{-6}) of the distance between Yb^{3+} and Er^{3+} ions.[58,59] The unit cell volume of the KM4 sample decreases with the increase of temperature, and lattice distortion occurs, resulting in a decrease in the distance between the sensitizer (*i.e.* Yb^{3+}) and the activator (*i.e.* Er^{3+}), and the ET between the lanthanide dopants is promoted, thus enhancing the UCL intensity of the

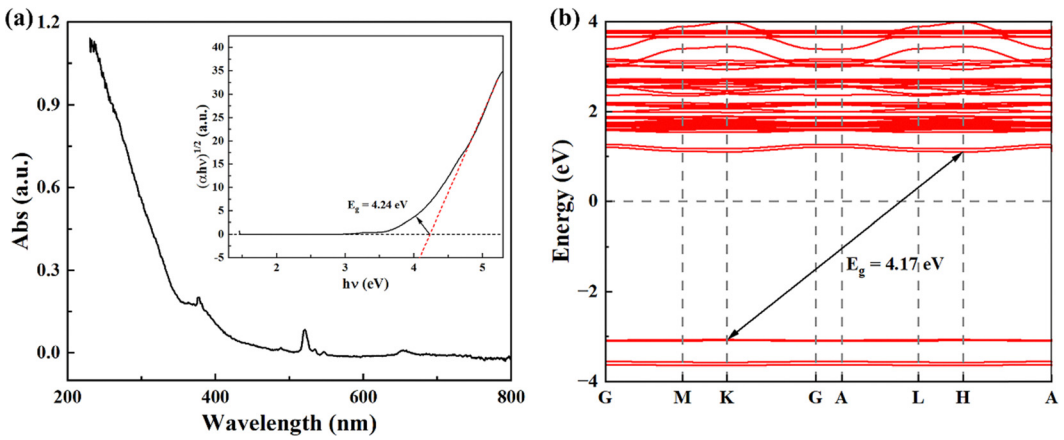

Fig. 5 (a) UV-vis absorption spectroscopy of the $KMgScW_3O_{12}$ sample; the inset shows the Tauc plot analyses to determine the optical band gap. (b) Calculated band structure of the $KMgScW_3O_{12}$ sample.

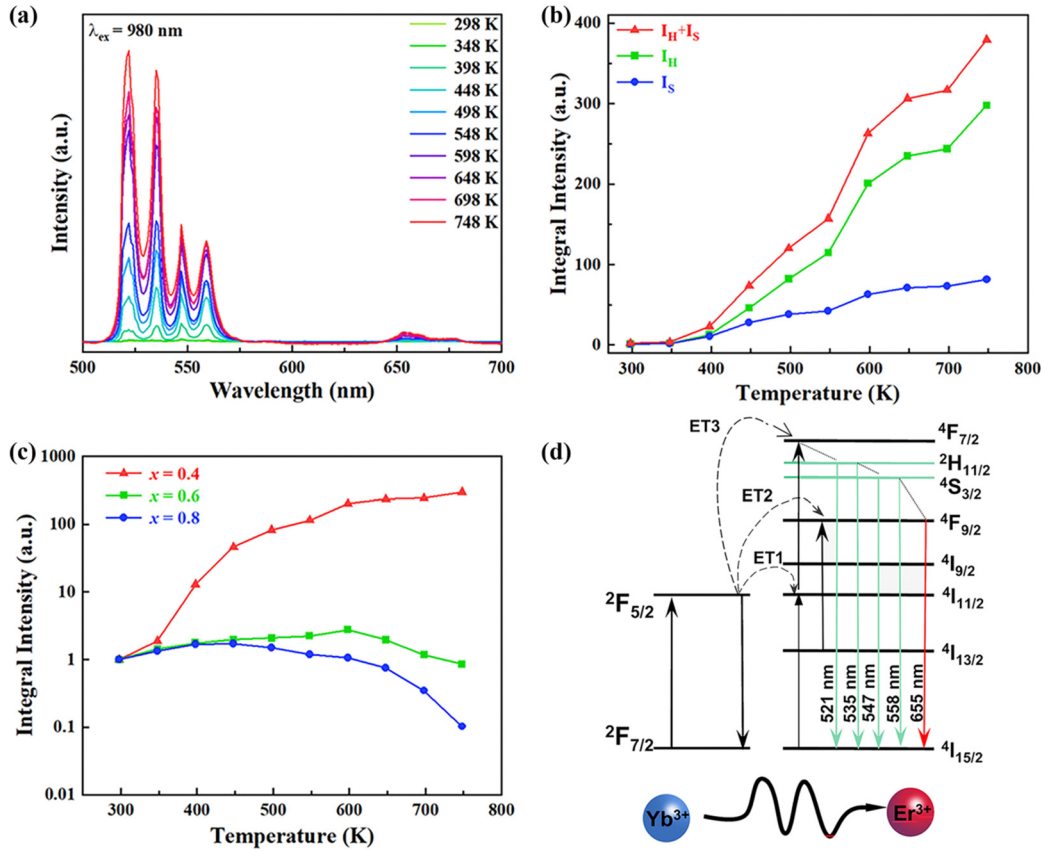

Fig. 6 (a) UCL emission spectra of the KM4 sample at 298–748 K under 980 nm laser excitation. (b) The corresponding UCL emission integral intensities of $^2H_{11/2(2)}/^2H_{11/2(1)}$, $^4S_{3/2(2)}/^4S_{3/2(1)}$ and total ($^2H_{11/2}$ + $^4S_{3/2}$) levels of Er^{3+} ions. (c) Integral intensity of KM4, KM6, and KM8 samples as a function of temperature. (d) Simplified energy level diagram to describe the ET process in the KM4 sample.

sample. The KM6 sample displays NTE (350–650 K) and PTE (650–800 K) (Fig. S3, ESI†). The sample shows luminescence thermal enhancement (RT-598 K), the total green UCL intensity is about 3.3 times that of RT, and then the sample shows

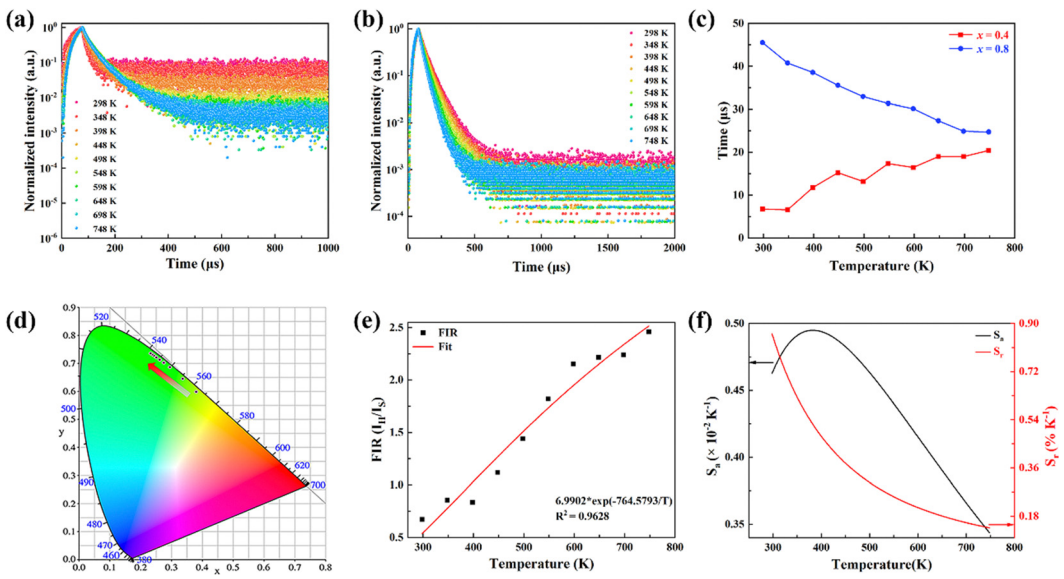

Fig. 7 The decay curves of (a) KM4 and (b) KM8 samples as a function of temperature. (c) The lifetimes of KM4 and KM8 samples as a function of temperature. (d) Commission Internationale de L'Eclairage (CIE) chromaticity diagram of the KM4 sample under 980 nm laser excitation. (e) The relationships between FIR values and sample temperature. (f) The absolute sensitivity S_a and relative sensitivity S_r curves.

luminescence TQ (598–748 K) (Fig. S6b, ESI†). Because the KM8 sample displays PTE (350–800 K) (Fig. S4, ESI†), the luminescence intensity of the sample should be quenched with the increase in temperature. The initial luminescence thermal enhancement may be due to the decrease of water molecules on the sample surface with increasing temperature, after which the PTE properties of the substance itself promote the TQ phenomenon of the sample (Fig. S7b, ESI†). Fig. 7(a)–(c) show the decay curves of KM4 and KM8 samples at 521 nm wavelength. Here we use the quadratic exponential function to get A_1, A_2, T_1, and T_2:

$$I_t = I_0 + A_1 e^{\frac{-t}{T_1}} + A_2 e^{\frac{-t}{T_2}} \quad (2)$$

where I_t represents the luminescence intensity at time t, I_0 represents the luminescence intensity at time 0, A_1 and A_2 are constants, t is the time, and T_1 and T_2 are short decay time and long decay time respectively. The effective average decay time of τ can be defined using the following equation:[60,61]

$$\tau = \frac{A_1 \cdot T_1^2 + A_2 \cdot T_2^2}{A_1 \cdot T_1 + A_2 \cdot T_2} \quad (3)$$

After fitting, the effective average decay time τ of the KM4 sample in Fig. 7(c) increases from 6.76 μs to 20.44 μs (298–748 K), and that of the KM8 sample decreases from 45.53 μs to 24.75 μs (298–748 K). The calculated trends of decay curves with the temperature of the two samples are consistent with the UCL spectra associated with the samples. The unit cell volume of the KM4 sample decreases with the increase of temperature, which makes the distance between Yb^{3+} and Er^{3+} ions decrease, thus improving the ET of Yb^{3+} ions and Er^{3+} ions and increasing the effective average decay time τ of the KM4 sample at 521 nm. According to the above analysis, the abnormal luminescence thermal enhancement characteristics of the sample are closely related to the NTE properties of the sample itself. The NTE properties of the sample can induce the phenomenon of luminescence thermal enhancement in the sample. The stronger the NTE of the sample, the better the luminescence performance of the sample. Therefore, the optimal ratio of the KM4 sample is selected for the next stage of the study.

The colour coordinates of the KM4 sample changed from (0.374, 0.565) to (0.238, 0.729) as the temperature increased, and the emitted green light became brighter and brighter (Fig. 7d), further indicating that the stronger the NTE characteristics, the much more the luminescence thermal enhancement behaviour. In general, using the FIR technique between TCLs from rare earth ions, UCL phosphors can be applied to achieve ratio thermometry.[62] It is of great significance for sensing applications to select suitable TCLs to study the relationship between luminescence intensity and temperature. The energy gap between $^2H_{11/2}$ and $^4S_{3/2}$ levels is 850 cm^{-1}, which is relatively suitable for thermal equilibrium. The ratio of the transition strength of $^2H_{11/2} \rightarrow {}^4I_{15/2}$ to that of $^4S_{3/2} \rightarrow {}^4I_{15/2}$ is different with the change of temperature, resulting in the FIR value being temperature dependent. Fig. 7(e) shows the relationship between FIR and temperature. From previous reports,[63,64] it can be clearly seen that the FIR value and TCLs have a good exponential relationship with temperature (*i.e.*, T), which is defined as follows:

$$I \propto gAhv \cdot e^{\frac{-E}{k_B T}} \quad (4)$$

$$\mathrm{FIR} = \frac{I_H}{I_S} = A \exp\left(-\frac{\Delta E}{k_B T}\right) \quad (5)$$

Eqn (4) and (5) describe the thermal equilibrium controlled by the Boltzmann factor, where g is the degeneracy of state, A is the spontaneous emissivity, h is Planck's constant, v is the frequency, E is the energy gap, k_B is the Boltzmann constant, and T is the absolute temperature.[28] In Fig. 7(e), the FIR (I_H/I_S) value is proportional to the sample temperature, and the FIR value increases significantly from 0.5411 at 298 K to 2.5170 at 573 K. According to the curve fitting in Fig. 7(e), the absolute sensitivity S_a can be defined using the following equation:[60]

$$S_a = \frac{\partial \mathrm{FIR}}{\partial T} = \mathrm{FIR} \cdot \frac{\Delta E}{k_B T^2} \quad (6)$$

The relative sensitivity S_r can be defined using the following formula:[30]

$$S_r = \frac{S_a}{\mathrm{FIR}} = \frac{\Delta E}{k_B T^2} \quad (7)$$

S_a and S_r are calculated from eqn (6) and (7). At 385 K, S_a has a maximum value of 0.50 × 10^{-2} K^{-1}, and at 298 K, S_r has a maximum value of 0.86% K^{-1} (Fig. 7f). The maximum S_a of the KM6 sample is 0.68 × 10^{-2} K^{-1} at 545 K, and S_r is maximum at 298 K, 1.22% K^{-1} (Fig. S6d, ESI†). The maximum S_a of the KM8 sample is 0.72 × 10^{-2} K^{-1} at 440 K, and the maximum S_r is 0.98% K^{-1} at 298 K (Fig. S7d, ESI†). The sensitivity of the rare-earth-doped fluorescent temperature sensor is compared in Table S7 (ESI†). The comparison shows that our material has a good relative sensitivity and a wide temperature range. In addition, it works well at high temperatures. Therefore, our material will be a potential candidate for high-temperature sensors.

3. Conclusions

In summary, the $(KMg)_xSc_{2-x}W_3O_{12}$-based compounds with space group $R\bar{3}c$ are synthesized using a solid-state reaction. They show NTE in the a/b axis and PTE in the c-axis. We can adjust the content of $(KMg)^{3+}$ to tailor the volumetric thermal expansion from positive to zero and negative. For an NTE material of KM4, the Sc5–O1–W3 bond angle decreases from 147° to 143.2°, and the Sc5–O2–W3 bond angle decreases from 152.3° to 145.8°, and extracting the distance between the nearest identical atoms, the distance between Sc atoms decreases, while the distance between W atoms increases, and NTE occurs in the ab plane. Besides, UV-vis absorption spectroscopy and DFT calculations show that the $KMgScW_3O_{12}$ sample is a wide-band gap semiconductor. KM4 shows the luminescence negative thermal quenching, while the PTE

sample of KM8 displays positive thermal quenching behaviour. The lifetimes of KM4 with NTE properties and KM8 with PTE properties are tested, and the trend of sample decay curves with temperature is consistent with the relevant UCL spectra. The NTE properties of the KM4 sample cause the lattice volume shrinkage with the increase in temperature, which improves the ET of Yb^{3+} to Er^{3+}, and thus the average lifetime τ of the KM4 sample at 521 nm increases. The NTE performance of the KM4 sample is the strongest and the time of luminescence thermal enhancement of this sample is the highest. The temperature sensing performance is studied in the range of 298–748 K. The maximum S_a is 0.50×10^{-2} K^{-1} at 385 K, and the maximum S_r is 0.86% K^{-1} at 298 K. These results show that we have not only discovered a new type of NTE material with adjustable CTE but also provide a new insight for the application of NTE materials in the field of luminescence.

Data availability

The data that support the findings of this study are openly available.

Conflicts of interest

There are no conflicts to declare.

Acknowledgements

This work was supported by the National Natural Science Foundation of China (Grant No. 22071221, 21905252, and 12204208), the Natural Science Foundation of Henan Province (No. 222301420040), and the Yunnan Fundamental Research Project (grant No. 202101BE070001-043). All calculations were supported by the National Supercomputing Center in Zhengzhou. We also thank the Center of Advanced Analysis & Gene Sequencing, Zhengzhou University, for the XRD test.

Notes and references

1 D. Barrera, J. A. O. Bruno, T. H. K. Barron and N. L. Allan, *J. Phys.: Condens. Mater.*, 2005, **17**, R217–R252.
2 E. Tallentire, F. Child, I. Fall, L. Vella-Zarb, I. R. Evans, M. G. Tucker, D. A. Keen, C. Wilson and J. S. O. Evans, *J. Am. Chem. Soc.*, 2013, **135**, 12849–12856.
3 X. Zhen, A. Sanson, Q. Sun, E. Liang and Q. Gao, *Phys. Rev. B*, 2023, **108**, 144102.
4 K. Greve, K. L. Martin, P. L. Lee, P. J. Chupas, K. W. Chapman and A. P. Wilkinson, *J. Am. Chem. Soc.*, 2010, **132**, 15496–15498.
5 Y. Qiao, S. Zhang, P. Zhang, J. Guo, A. Sanson, X. Zhen, K. Zhao, Q. Gao and J. Chen, *Nano Res.*, 2024, **17**, 2195–2203.
6 Q. Gao, J. Chen, Q. Sun, D. Chang, Q. Huang, H. Wu, A. Sanson, R. Milazzo, H. Zhu, Q. Li, Z. Liu, J. Deng and X. Xing, *Angew. Chem., Int. Ed.*, 2017, **56**, 9023–9028.
7 Q. Gao, Y. Jiao, Q. Sun, J. Sprenger, M. Finze, A. Sanson, E. Liang, X. Xing and J. Chen, *Angew. Chem., Int. Ed.*, 2024, **13**, e202401302.
8 H. N. Rimmer, M. T. Dove, A. L. Goodwin and D. C. Palmer, *Phys. Chem. Chem. Phys.*, 2014, **16**, 21144–21152.
9 I. Grobler, V. J. Smith, P. M. Bhatt, S. A. Herbert and L. J. Barbour, *J. Am. Chem. Soc.*, 2013, **135**, 6411–6414.
10 M. Azuma, W.-T. Chen, H. Seki, M. Czapski, S. Olga, K. Oka, M. Mizumaki, T. Watanuki, N. Ishimatsu, N. Kawamura, S. Ishiwata, M. G. Tucker, Y. Shimakawa and J. P. Attfield, *Nat. Commun.*, 2011, **2**, 347.
11 Y. Long, T. Saito, T. Tohyama, K. Oka, M. Azuma and Y. Shimakawa, *Inorg. Chem.*, 2009, **48**, 8489–8492.
12 C. Wang, L. Chu, Q. Yao, Y. Sun, M. Wu, L. Ding, J. Yan, Y. Na, W. Tang, G. Li, Q. Huang and J. W. Lynn, *Phys. Rev. B: Condens. Matter Mater. Phys.*, 2012, **85**, 220103.
13 J. Cliffe, J. A. Hill, C. A. Murray, F.-X. Coudertc and A. L. Goodwin, *Phys. Chem. Chem. Phys.*, 2015, **17**, 11586–11592.
14 A. Mary, J. S. O. Evans, T. Vogt and A. W. Sleight, *Science*, 1996, **272**, 90–92.
15 M. Förster and A. W. Sleight, *Int. J. Inorg. Mater.*, 1999, **1**, 123–127.
16 J. Chen, Q. Gao, A. Sanson, X. Jiang, Q. Huang, A. Carnera, C. G. Rodriguez, L. Olivi, L. Wang, L. Hu, K. Lin, Y. Ren, Z. Lin, C. Wang, L. Gu, J. Deng, J. P. Attfield and X. Xing, *Nat. Commun.*, 2017, **8**, 14441.
17 R. Hester, J. C. Hancock, S. H. Lapidus and A. P. Wilkinson, *Chem. Mater.*, 2017, **29**, 823–831.
18 A. Marinkovic, P. I. Pontón, C. P. Romao, T. Moreira and M. A. White, *Front. Mater.*, 2021, **8**, 741560.
19 H. Liu, W. Sun, Z. Zhang, L. N. Lovings and C. Lind, *Solids*, 2021, **2**, 87–107.
20 J. Miller, C. P. Romao, M. Bieringer, B. A. Marinkovic, L. Prisco, M. A. White and L. Pinckney, *J. Am. Ceram. Soc.*, 2013, **96**, 561–566.
21 K. Tyagi, S. N. Achary and M. D. Mathews, *J. Alloys Compd.*, 2002, **339**, 207–210.
22 X. Liu, Y. Cheng, E. Liang and M. Chao, *Phys. Chem. Chem. Phys.*, 2014, **16**, 12848–12857.
23 O. Hagman, P. Kierkegaard, P. Karvonen, A. I. Virtanen and J. Paasivirta, *Acta Chem. Scand.*, 1968, **22**, 1822–1832.
24 E. Breval, H. A. McKinstry and D. K. Agrawal, *J. Mater. Sci.*, 2000, **35**, 3359–3364.
25 I. Pet'Kov and A. I. Orlova, *Inorg. Mater.*, 2003, **39**, 1013–1023.
26 B. Angadi, V. M. Jali, M. T. Lagare, N. S. Kini and A. M. Umarji, *Bull. Mater. Sci.*, 2002, **25**, 191–196.
27 H. Liu, H. Wang, X. Zheng, P. Wang and Y. Zhang, *Dalton Trans.*, 2022, **51**, 13106–13118.
28 X. Qin, J. Xu, Y. Wu and X. Liu, *ACS Cent. Sci.*, 2019, **5**, 29–42.
29 C. Homann, L. Krukewitt, F. Frenzel, B. Grauel, C. Würth, U. Resch-Genger and M. Haase, *Angew. Chem., Int. Ed.*, 2018, **57**, 8765–8769.
30 V. Morozov, S. Zhang, M. C. Brennan, B. Janko and M. Kuno, *ACS Energy Lett.*, 2017, **2**, 2514–2515.

31 X. Yan and Y. D. Li, *Adv. Funct. Mater.*, 2005, **15**, 763–770.
32 J. Zou, B. Chen, Y. Hu, Q. Zhang, X. Wang and F. Wang, *J. Phys. Chem. Lett.*, 2020, **11**, 3020–3024.
33 J. Liao, M. Wang, F. Lin, Z. Han, B. Fu, D. Tu, X. Chen, B. Qiu and H.-R. Wen, *Nat. Commun.*, 2022, **13**, 2090.
34 J. Huang, Z. Han, B. Fu, H. Yan, J. Liao, G. Gong and H.-R. Wen, *Mater. Today Commun.*, 2022, **33**, 104548.
35 Y. Wei, Y. Pan, E. Zhou, Z. Yuan, H. Song, Y. Wang, J. Zhou, J. Rui, M. Xu, L. Ning, Z. Liu, H. Wang, X. Xie, X. Tang, H. Su, X. Xing and L. Huang, *Angew. Chem., Int. Ed.*, 2023, **135**, e202303482.
36 M. Seshadri, M. Radha, M. J. V. Bell and V. Anjos, *Ceram. Int.*, 2018, **44**, 20790–20797.
37 R. Dousti, R. J. Amjad, R. Hosseinian, M. Salehi and M. R. Sahar, *J. Lumin.*, 2015, **159**, 100–104.
38 R. Balda, V. Seznec, V. Nazabal, J. L. Adam, M. Al-Saleh and J. Fernández, *J. Non-Cryst. Solids*, 2006, **352**, 2444–2447.
39 A. Woodcock and P. Lightfoot, *J. Mater. Chem.*, 1999, **9**, 2907–2911.
40 L. Hu, J. Chen, L. Fan, Y. Ren, Y. Rong, Z. Pan, J. Deng, R. Yu and X. Xing, *J. Am. Chem. Soc.*, 2014, **136**, 13566–13569.
41 W. Chapman, P. J. Chupas and C. J. Kepert, *J. Am. Chem. Soc.*, 2006, **128**, 7009–7014.
42 S. Margadonna, K. Prassides and A. N. Fitch, *J. Am. Chem. Soc.*, 2004, **126**, 15390–15391.
43 M. Li, Y. Li, C.-Y. Wang and Q. Sun, *Chin. Phys. Lett.*, 2019, **36**, 066301.
44 M. Kozhevnikova and T. N. Khamaganova, *Russ. J. Inorg. Chem.*, 2008, **53**, 800–804.
45 P. Salke, M. K. Gupta, R. Rao, R. Mittal, J. Deng and X. Xing, *J. Appl. Phys.*, 2015, **117**, 235902.
46 A. Sanson, M. Giarola, G. Mariotto, L. Hu, J. Chen and X. Xing, *Mater. Chem. Phys.*, 2016, **180**, 213–218.
47 Y. Gao, C. Wang, Q. Gao, J. Guo, M. Chao, Y. Jia and E. Liang, *Inorg. Chem.*, 2020, **59**, 18427–18431.
48 Y. Liu, D. Mei, N. Wang, M. S. Molokeev, X. Jiang and Z. Lin, *ACS Appl. Mater. Interfaces*, 2020, **12**, 38435–38440.
49 Q. Gao, Q. Sun, A. Venier, A. Sanson, Q. Huang, Y. Jia, E. Liang and J. Chen, *Sci. China Mater.*, 2022, **65**, 553–557.
50 Y. Liu, D. Mei, N. Wang, M. S. Molokeev, X. Jiang and Z. Lin, *ACS Appl. Mater. Inter.*, 2020, **12**, 38435–38440.
51 C. S. Tauc, R. Grigorovici and A. Vancu, *Phys. Status Solidi B*, 1966, **15**, 627–637.
52 S. Wang and B. M. Klein, *Phys. Rev. B: Condens. Matter Mater. Phys.*, 1981, **24**, 3393–3416.
53 N. Niu, P. Yang, F. He, X. Zhang, S. Gai, C. Li and J. Lin, *J. Mater. Chem.*, 2012, **22**, 10889–10899.
54 N. Niu, F. He, S. Gai, C. Li, X. Zhang, S. Huang and P. Yang, *J. Mater. Chem.*, 2012, **22**, 21613–21623.
55 H. Lu, R. Meng, H. Hao, Y. Bai, Y. Gao, Y. Song, Y. Wang and X. Zhang, *RSC Adv.*, 2016, **6**, 57667–57671.
56 F. Wang, Y. Han, C. S. Lim, Y. Lu, J. Wang, J. Xu, H. Chen, C. Zhang, M. Hong and X. Liu, *Nature*, 2010, **463**, 1061–1065.
57 J. Qiao, L. Ning, M. S. Molokeev, Y.-C. Chuang, Q. Liu and Z. Xia, *J. Am. Chem. Soc.*, 2018, **140**, 9730–9736.
58 W. Lin, X. Bai, B. Zhu, S. Yan, K. Ruan, X. Cai, Z. Ding, B. Zhang, I. Khan, A. A. Haider, J. Qiu, Z. Song, A. Huang, Y. Cun, C. Tatiana and Z. Yang, *Ceram. Int.*, 2023, **49**, 38247–38255.
59 B. Barthem and R. Buisson, *J. Lumin.*, 1988, **40**, 637–638.
60 Y. Wu, T. He and L. Lun, *J. Photochem. Photobiol., A*, 2019, **376**, 135–139.
61 M. Müller and T. Jüstel, *J. Lumin.*, 2014, **155**, 398–404.
62 H. Cui, Y. Cao, Y. Zhang, T. Peng, L. Cao, S. Ran, Y. Wang, D. Wu, X. Li, X. Zhang and B. Chen, *Ceram. Int.*, 2021, **47**, 21271–21275.
63 M. Sójka, J. F. C. B. Ramalho, C. D. S. Brites, K. Fiaczyk, L. D. Carlos and E. Zych, *Adv. Opt. Mater.*, 2019, **7**, 1901102.
64 M. Runowski, N. Stopikowska, D. Szeremeta, S. Goderski, M. Skwierczyńska and S. Lis, *ACS Appl. Mater. Interfaces*, 2019, **11**, 13389–13396.

